Ultrafast charge–discharge characteristics of a nanosized core–shell structured LiFePO$_4$ material for hybrid supercapacitor applications†

Katsuhiko Naoi,*[abcd] Kazuaki Kisu,[ad] Etsuro Iwama,[ad] Shota Nakashima,[a] Yuki Sakai,[a] Yuki Orikasa,[e] Philippe Leone,[f] Nicolas Dupré,[f] Thierry Brousse,[dfg] Patrick Rozier,[dgh] Wako Naoi[c] and Patrice Simon[dgh]

Highly dispersed crystalline/amorphous LiFePO$_4$ (LFP) nanoparticles encapsulated within hollow-structured graphitic carbon were synthesized using an *in situ* ultracentrifugation process. Ultracentrifugation triggered an *in situ* sol–gel reaction that led to the formation of core–shell LFP simultaneously hybridized with fractured graphitic carbon. The structure has double cores that contain a crystalline LFP (core 1) covered by an amorphous LFP containing Fe^{3+} defects (core 2), which are encapsulated by graphitic carbon (shell). These core–shell LFP nanocomposites show improved Li$^+$ diffusivity thanks to the presence of an amorphous LFP phase. This material enables ultrafast discharge rates (60 mA h g^{-1} at 100C and 36 mA h g^{-1} at 300C) as well as ultrafast charge rates (60 mA h g^{-1} at 100C and 36 mA h g^{-1} at 300C). The synthesized core–shell nanocomposites overcome the inherent one-dimensional diffusion limitation in LFP and yet deliver/store high electrochemical capacity in both ways symmetrically up to 480C. Such a high rate symmetric capacity for both charge and discharge has never been reported so far for LFP cathode materials. This offers new opportunities for designing high-energy and high-power hybrid supercapacitors.

Broader context

This paper presents the synthesis of a novel nano-structured core (LiFePO$_4$)/shell (graphitic carbon) material that shows ultrafast discharge and charge performance (beyond the 300C rate), for high power delivery for supercapacitor applications. These unique features originate from the structure of the nanocomposite that contains a core of crystalline LFP covered by amorphous, defective LFP, all encapsulated in a graphitic carbon shell, prepared using an *in situ* ultracentrifugation (UC) process. Such high charge/discharge rates with similar capacity have never been reported so far for LiFePO$_4$ cathode materials. The reason for this high rate performance comes from fast lithium-ion diffusion and high electrical conductivity characteristics conferred by the core–shell nanocomposite. With great interest in electrochemical energy storage, the ability to increase kinetics and achieve charge/discharge in less than 1 minute will have a substantial impact on the field. The fact that these results are achieved in practical electrode structures for use in electrochemical capacitor devices will also be of interest to the community.

[a] Department of Applied Chemistry, Tokyo University of Agriculture & Technology, 2-24-16 Naka-cho, Koganei, Tokyo 184-8588, Japan. E-mail: k-naoi@cc.tuat.ac.jp

[b] Advanced Capacitor Research Center, Tokyo University of Agriculture & Technology, 2-24-16 Naka-cho, Koganei, Tokyo 184-8588, Japan

[c] Division of Art and Innovative Technologies, K & W Inc, 1-3-16-901 Higashi, Kunitachi, Tokyo 186-0002, Japan

[d] Global Innovation Research Organization, Tokyo University of Agriculture & Technology, 2-24-16 Naka-cho, Koganei, Tokyo 184-8588, Japan

[e] Graduate School of Human and Environment Studies, Kyoto University, Yoshida-nihonmatsu-cho, Sakyo-ku, Kyoto 606-8501, Japan

[f] Institut des Matériaux Jean Rouxel (IMN), UMR 6502, Université de Nantes, CNRS, rue Christian Pauc, BP50609, 44306 Nantes Cedex 3, France

[g] Réseau sur le Stockage Electrochimique de l'Energie (RS2E), FR CNRS 3459, France

[h] CIRIMAT, Université de Toulouse, CNRS, INPT, UPS, 118 route de Narbonne 31062 Toulouse cedex 9, France

† Electronic supplementary information (ESI) available. See DOI: 10.1039/c6ee00829a

1. Introduction

The development of power electronics as well as the growing need for portable and mobile electronic devices highlight the need for high performance electrochemical energy storage sources. Intensive research efforts are currently made to improve battery performance by designing advanced materials based on the Li-ion[1] or new chemistries.[2] Batteries can provide high energy density, thus ensuring autonomy, but fail to deliver high power peaks needed for many applications.[3] As a result, electrochemical capacitors (ECs), also called supercapacitors, have been attracting attention due to their much greater power density and cyclability as compared to batteries.[4] Conventional ECs store the charge by ion adsorption at high surface-area porous carbon electrodes.

Such an electrostatic charge storage mechanism limits the capacitance of the carbonaceous materials, thus limiting the energy density of the devices. One way to increase the energy density of ECs is to move from an electrostatic to a pseudocapacitive charge storage mechanism.

Pseudo-capacitance[5] arises from a fast redox reaction at the surface of materials. RuO_2,[6] MnO_2,[7] oxides with spinel structures,[8] or some metal nitrides[9] are well-known examples of pseudocapacitive materials, which have been described in the literature. Various strategies have been proposed for improving their performance, including nanostructuration,[10] deposition onto high-surface area materials like graphene, carbon nanotubes or porous carbons[11] and the control of crystallographic structure.[12] However, most of the pseudocapacitive materials operate in aqueous electrolytes, thus limiting their practical interest for high-energy supercapacitor applications. Recently, in a non-aqueous electrolyte, a specifically designed orthorhombic Nb_2O_5 material used as a negative electrode has shown intrinsic capacitive features with extremely high power performance.[13] Therefore Li^+ intercalation was achieved by the pseudocapacitive mechanism. Nano-sizing of battery materials is also known to enhance their power performance.[14] However, despite nano-sized $Li_4Ti_5O_{12}$,[15] $TiO_2(B)$,[16] $LiCoO_2$,[17] and V_2O_5[18] demonstrating higher power and capacity than the bulk materials, a major concern is that nanostructured forms exhibit irreversible capacity loss during cycling. In addition, since the exposure of the surface to the electrolyte is a critical factor, preparation of conventional composite electrode architectures with binders is difficult to achieve because of a decrease in the surface area and a poor electrical percolation network.[10]

$LiFePO_4$ (lithium iron phosphate, LFP) has long been investigated as a cathode material in Li-ion batteries because of its high theoretical capacity of 170 mA h g^{-1}, low cost and high electrochemical and thermal stabilities.[19] An electrochemical reaction of LFP proceeds through a two-phase reaction between Li-rich $Li_{1-a}FePO_4$ (LFP) and Li-poor Li_bFePO_4 (FP)[20] with Li insertion/deinsertion occurring along the b axis.[21] However, the limited diffusion kinetics of Li ions at the LFP/FP interface together with the poor electronic conductivity of the pristine olivine-LFP (10^{-10} to 10^{-7} Ω^{-1} cm^{-1})[22] limit the power capability of the material. Downsizing the particle size (5–100 nm) failed to enhance the power performance due to the re-aggregation of particles and the difficulty in creating efficient electron pathways.[23] The synthesis of carbon coatings onto LFP particles has also been proposed, by adding carbon precursors during the synthesis of LFP.[24–26] However, non-conformal amorphous carbon coatings did not show enough improvement in electrical conductivity when nano-sized LFP particles were prepared.[27]

In this paper, we report on the synthesis of single nanosized LFP crystals encapsulated within hollow-structured graphitic carbons by an *in situ* ultracentrifugation (UC)[28,29] process for hybrid supercapacitor applications. The composite material has a core LFP (crystalline (core 1)/amorphous (core 2))/graphitic carbon shell structure that offers both high reversibility and high rate capability. The electrochemical properties and performance of the LFP/graphitic carbon material showed outstanding high rate and capacity retention with a capacity of more than 24 mA h g^{-1} at a 480C discharge or charge rate (7.5 seconds). Such results pave the way for designing high energy and high power materials to be used in hybrid supercapacitors.[30]

2. Results and discussion

2.1. Structural characterization

The Scanning Electron Microscope (SEM) image of the LFP/graphic carbon composite shows uniformly dispersed 30 nm-diameter spheres (Fig. 1a and Fig. S1a, ESI†). Transmission Electron Microscope (TEM) experiments show that they are made of a core of LFP particles with the size between 10 and 20 nm as evidenced using dark field images (white spots in Fig. 1c). These particles are encapsulated in a 5 nm thick carbon shell visible as a grey region in both bright (Fig. 1b and Fig. S1b, ESI†) and dark (Fig. 1c and Fig. S1c, ESI†) field images.

X-ray photoelectron spectroscopy (XPS) analysis of the Fe $2p_{3/2}$ energy level was performed on samples obtained. The XPS data obtained after increasing the duration of Ar-ion etching show that above 20 s a slight intensity at 708 eV appears (Fig. S2, ESI†). This is the evidence of the presence of Fe^0 indicating that Ar-ion etching has brought about an unwanted reduction of Fe species to the metal state thus destroying the LFP compound. Therefore, we used the data within 14 s that would be reasonable to judge the valence of Fe as a function of depth of the
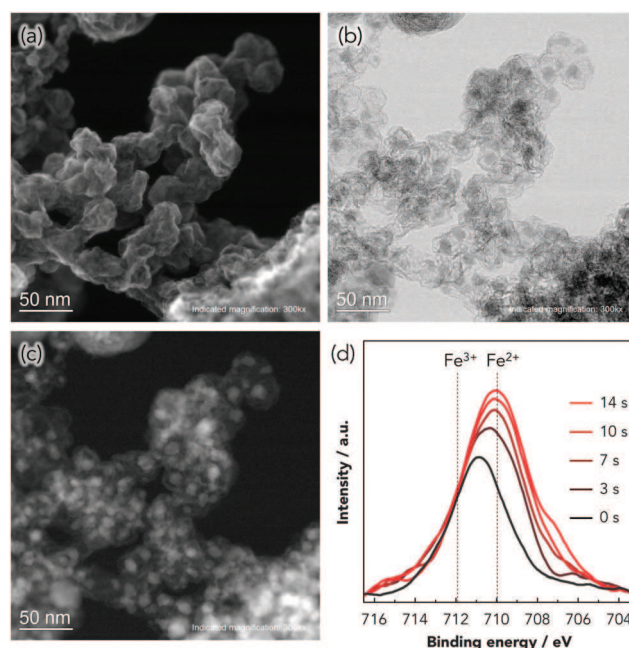

Fig. 1 (a) Scanning electron microscope (SEM), (b) bright-field, and (c) dark-field images of the UC-derived LFP/graphitic carbon composites represent a unique nanostructure of two phases, whereby each spherical LFP core is accommodated/encapsulated within the hollow structured graphitic carbon shells. (d) Consecutive XPS (Fe 2p core peaks) measurements with data acquisition at 1 s intervals during 0–14 s Ar ion etching, representing a depth profile of the same sample to ensure that the peculiar core–shell structure of our LFP/graphitic carbon composites was derived from ultracentrifugation.

composite (Fig. 1d). The XPS spectrum of the surface of the composite (0 s) shows a peak with a maximum at 711.2 eV, that contains signals of Fe^{2+} (LFP; 710 eV) and Fe^{3+} (FP; 712 eV)[31] in almost equivalent amount. The spectra obtained on samples with increasing etching duration (increasing depth in the composite) show an increase of the peak intensity and a shift of the peak position up to 710.1 eV. The increase of the intensity well agrees with the previous SEM and HRTEM observations of the encapsulation of the Fe-containing particle by a graphitic carbon hollow structure. The gradual shift of the peak evidences that the LFP core contains a Fe^{2+} and Fe^{3+} mixture with a Fe^{3+}/Fe^{2+} ratio changing from the surface to the core of the particle, the latter corresponding to pure Fe^{2+}. The analysis of the valence states by Fe Mössbauer spectroscopy (Fig. 2a and Table S1, ESI†) confirms the presence of both Fe^{2+} and Fe^{3+} valence states in an atomic ratio of 53/47. The deconvolution of the spectrum shows that only one contribution for Fe^{3+} is observed (blue line) while two contributions have to be taken into account for the Fe^{2+} one (red line) corresponding to undistorted M2 sites (14%) and the second (green line) to distorted M2 sites (40%).[32,33]

An X-ray diffraction study was conducted to crosscheck the crystallographic information on the LFP/graphitic carbon
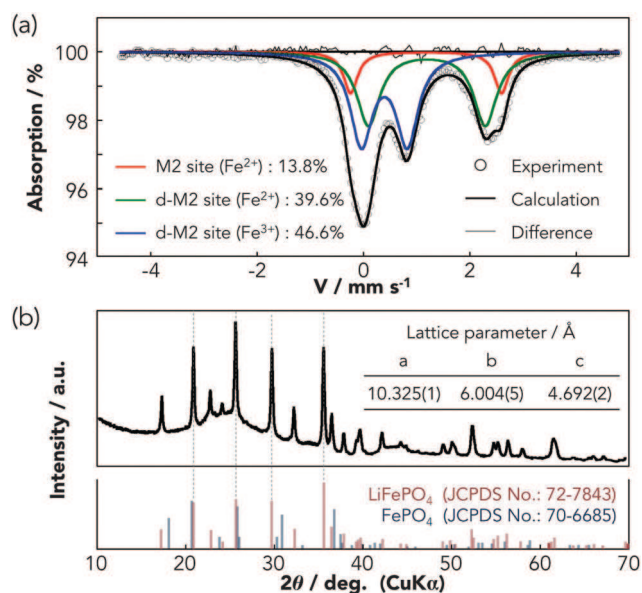

Fig. 2 Structural characterization of the same LFP/graphitic carbon composite as in Fig. 1. (a) Mössbauer spectrum fitted with three Fe environments (Fe^{2+}, disordered Fe^{2+}, and disordered Fe^{3+}), suggesting that the LFP/graphitic carbon composite contains amorphous LFP with Fe^{3+} defects. (b) XRD patterns of the same LFP/graphitic carbon composite. The major diffraction peaks ((101), (111), (211), and (301)) of the XRD patterns are well indexed to the orthorhombic structure of $LiFe(II)PO_4$ with the *Pnma* space group (JCPDS card No. 72-7843). No peaks due to $Fe(III)PO_4$ appear in the XRD pattern, suggestive of the existence of an amorphous phase $Fe(III)PO_4$. A broad peak observed at around 24.5° corresponds to the (002) plane of KB. This result indicates that the obtained LFP/graphitic carbon composite did not have any impurities such as FeP and $Li_3Fe_2(PO_4)_3$. The Scherrer equation was applied to the strongest three peaks corresponding to (104), (110), and (116) planes for LFP. The average crystal size was determined to be 39 nm for LFP, suggesting that nano-LFP particles were synthesized by UC treatment.

composite (Fig. 2b). All diffraction peaks were indexed in the orthorhombic lattice of LFP (JCPDS card 72-7845) showing that no crystalline impurity is detected. The cell parameters, refined using the profile matching method, are $a = 10.325(1)$ Å, $b = 6.004(5)$ Å, $c = 4.692(2)$ Å, and $V = 290.9(1)$ Å^3 in accordance with the reported values for conventional LFP materials ($V = 291.2$ Å^3)[34,35] and clearly higher than the reported ones for highly defective LFP[33] ($V = 286.8$ Å^3 for 44 at% of Fe^{3+}). The lowering of the unit cell volume being related to the shortening of Fe–O bonds with the increase of the Fe valence state, the slight (0.1%) decrease observed compared to the high amount of Fe^{3+} (47%) suggests that most of the Fe^{3+} are included in an amorphous phase.

TEM experiments are in accordance with the existence of such an amorphous phase. The TEM images (see Fig. 3 and Fig. S3, ESI†) show that the sample is constituted of three parts. A crystalline core (*ca.* 12–15 nm diameter), an intermediate amorphous layer (*ca.* 2–5 nm thick) (core 2 in light purple) and an outermost shell layer (*ca.* 5 nm thick) composed of more or less randomly distributed units. The analysis of the crystalline core (core 1) shows an interplanar lattice distance of $d = 0.42$ nm corresponding to the (101) plane of the olivine LFP (Fig. 3a) and the outermost shell layer shows an inter unit distance of $d = 0.35$ nm a little larger than that of graphene. This confirms that the sample contains a crystalline LFP core surrounded by an amorphous phase, both being encapsulated in randomly organized (KB derived) carbon graphitic units stacked onto each other. Based on the combination of the different experiments it can be assumed that the amorphous layer contains most of the Fe^{3+} ions; it will be named as "amorphous defective LFP" in the following. The composite contains 48% of LFP and 52% of graphitic carbon (Fig. S4, ESI†). Elemental mapping obtained from electron energy loss spectroscopy (Fig. S5, ESI†) shows that iron, phosphorus, and oxygen are localized in the whole core–shell particles, while Li is distributed over a larger area (Fig. S6, ESI†) including the carbon part. While the average composition is in accordance with the expected one for LFP/C composites, the specific distribution of Li in the whole sample accounts for the partial oxidation of Fe^{2+} up to Fe^{3+}. In addition, thermal gravimetric analysis (TGA) of the LFP/graphitic carbon composite shows a decrease of the decomposition temperature of the carbon (Fig. S4, ESI†), confirming a close interaction between the LFP and the graphitic carbon shell. Thus it can be expected that the combination of KB and UC treatment allows a partial oxidation of pristine LFP which would explain that Fe^{3+} concentration increases from the core to the surface of the particles leading, for highly defective LFP, to an amorphization of the sample. A sample containing only LFP (without KB) was prepared under the same UC conditions. The uc-LFP material resulted in a large or agglomerated crystal as shown in Fig. S7b (ESI†) that does not exhibit such a peculiar core–shell structure (Fig. S7a, ESI†). The composite was also thermally treated to remove the graphitic carbon shell under an air atmosphere at 700 °C. This experiment resulted in substantial agglomeration and increased particle size (Fig. S7c, ESI†). Therefore, the role of the carbon shell is clearly very
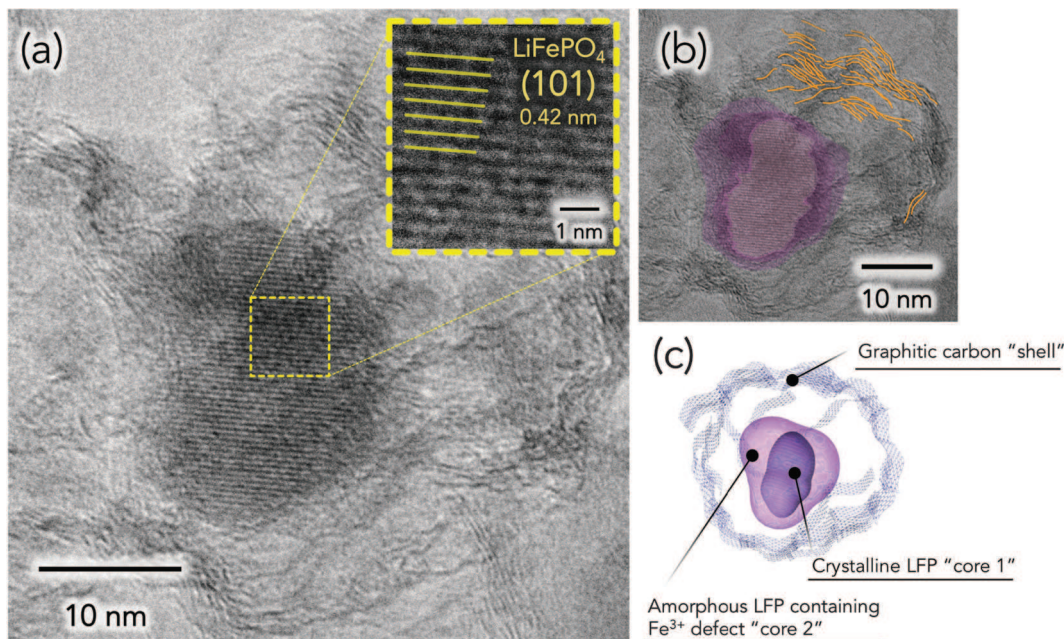
Fig. 3 (a) Higher-magnification HRTEM image of the LFP/graphitic carbon composite featuring crystalline LFP nanoparticles (*ca.* 15 nm) with clear lattice fringes (*d* = 0.42 nm; LFP(101)) encapsulated within the random graphene fragments derived from high-surface-area KB graphitic carbons. (b) Magnified HRTEM image of the LFP/graphitic carbon composite with a marker for each component. (c) Schematic illustration of the core−shell nanostructure of the LFP/graphitic carbon composite, representing a minute structure consisting of an amorphous outer sphere of a LFP containing Fe^{3+} defects and an inner sphere of crystalline LFP.

important to maintain the peculiar nano-sized "core–shell" structure to sustain ultrafast electrochemical performance (see later Section 2.3).

2.2. Combined electrochemical and *in situ* XAFS and XRD characterization of LFP/graphitic carbon composites

The electrochemical behavior of the LFP/graphitic carbon composite was investigated in half-cells *versus* Li anode at 1C rate (1C = 170 mA g^{-1}) (Fig. 4). At the 1st charge, a low capacity of 54 mA h g^{-1} of composite is obtained, that is 87 mA h g^{-1} of LFP. This corresponds to 0.51 Li extracted per LFP after subtracting the double layer capacitance contribution of the UC treated KB (uc-KB) (24 mA h g^{-1}, Fig. S8, ESI†). After the 1st discharge process, a reversible capacity of 96 mA h g^{-1} per composite is obtained, corresponding to 134 mA h g^{-1} of LFP and 0.78 Li-ion intercalated per LFP, after removing the reversible capacity of uc-KB at the 1st discharge (63 mA h g^{-1}). The presence of Fe^{3+} in the as-prepared composite explains the difference between charge and discharge capacity at the 1st cycle. This confirms the previous results from Mössbauer analysis, showing 53% of Fe^{2+} and 47% of Fe^{3+} in the pristine LFP/graphitic carbon composite. After the 1st charge/discharge cycle, the reversible capacity is increased to 140 mA h g^{-1} of LFP, corresponding to 0.82 Li exchanged per LFP. Long-life cycling performance of the composite was investigated. We have cycled more than 2000 times at 10C (Fig. 4 (inset)), 60C and 240C (Fig. S9, ESI†). The retention of the discharge capacity was 85, 92 and 96% for 10, 60 and 240C, respectively. Such cycling performance positively compares with other reports on LFP nanoparticles.[25,36,37]
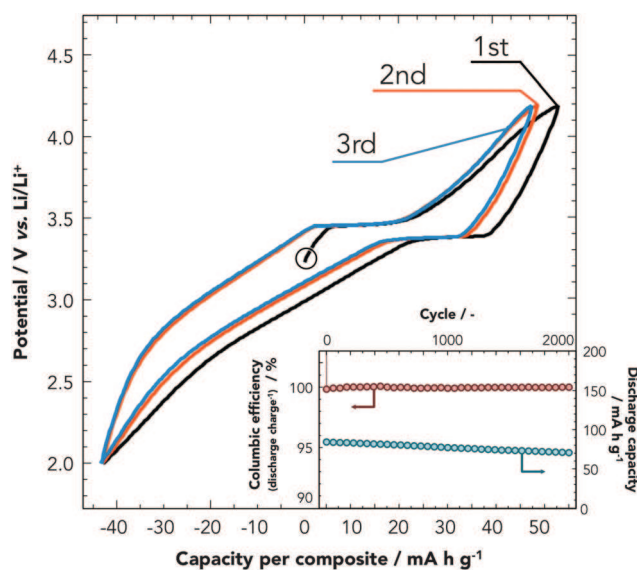

Fig. 4 Charge−discharge curves (1st−3rd cycle) of a half-cell consisting of Li/1 M $LiPF_6$ EC + DEC (LFP/graphitic carbon) composite at a 1C rate. Inset: Retention of discharge capacity over 1−2000 cycles at 10C rate.

The electrochemical signature of the composite shows three various regions: a plateau at 3.4 V and sloping profiles above and below ∼3.4 V. The plateau corresponds to the conventional two-phase reaction observed for crystalline-LFP. A small polarization of only 100 mV at 1C is measured, suggesting that the presence of the amorphous defective LFP phase does not hinder Li diffusion along the [100] channels. Below 3.4 V,

as mentioned previously, the potential changes with the electrode capacity. Amisse *et al.* have recently reported such a sloping profile with highly defective crystalline LFP phase containing 44% of Fe^{3+}.[33] They attributed this signature to the redox activity of Fe^{2+} and Fe^{3+} in distorted M2 sites. Considering, in the present paper, that the reversible capacity of the uc-KB is only 30 mA h g^{-1} below 3.4 V (Fig. S8, ESI†), 75% of the capacity below 3.4 V can be assigned to the redox activity of the Fe^{3+} defects in the pristine composite.

To confirm this, the redox states of Fe were investigated by *in situ* X-ray absorption measurements during cycling. The X-ray absorption near-edge structure (XANES) spectra of the Fe K-edge for the LFP/graphitic carbon composites are shown in Fig. 5a (insets) during the 1st cycle. The threshold energy position of the Fe K-edge absorption gives information about the valence state of the probing atom. The average valence state of Fe in the composite is determined by the deconvolution of the spectra using the contributions of Fe^{2+} and Fe^{3+} (see the ESI†). Fig. 5a shows the changes of the valence numbers of Fe during charge–discharge at 0.1C rate. At 3.1 V (OCV), the initial valence state of Fe is +2.5, in good agreement with the previous Mössbauer spectroscopy results (Fig. 2a). During the 1st delithiation process, from runs 1 to 15, the valence state linearly increases from +2.50 to +2.89 in the plateau domain (up to run 10) while in the sloping region from 3.4 V to 4.2 V, the redox state of Fe is kept almost constant (runs 10 to 15). Then, during the 1st lithiation, the Fe valence state is similarly almost constant above 3.4 V (runs 15 to 18). This indicates that the charge storage mechanism beyond 3.4 V does not involve redox reaction, but double layer capacitance from the graphitic carbon shell. Further, the valence state linearly decreases from 3.4 V (run "18") down to 2.5 V (run "33") and the capacity is associated with the reduction of Fe from (+2.89) down to (+2.14). Below 2.5 V, the Fe valence is almost unchanged (runs 33 to 36), showing a major contribution of the double layer capacitance from the graphitic carbon shell. During the 2nd charge, the Fe valence state increases with increasing potential. The valence number of Fe varies symmetrically during the 1st discharge (runs 15 to 36) and 2nd charge
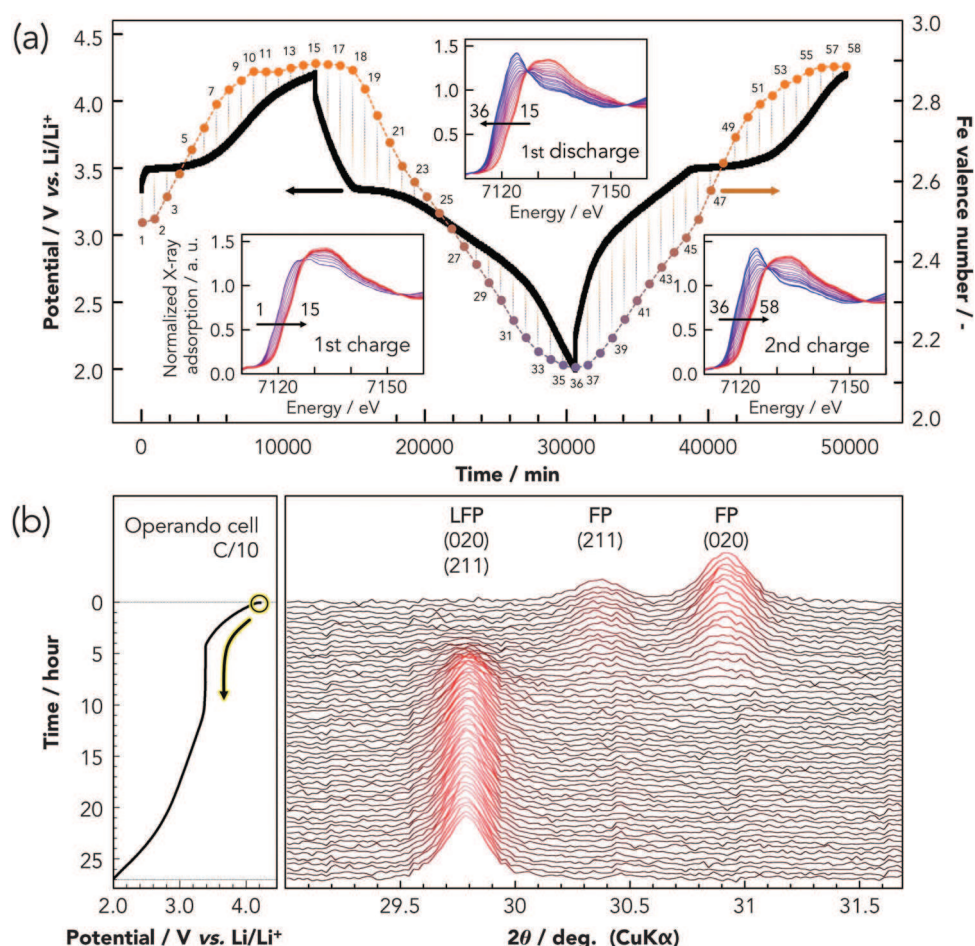

Fig. 5   *In situ* XAFS and XRD measurements on a half-cell consisting of Li/1 M LiPF$_6$ EC + DEC (LFP/graphitic carbon) composites. (a) Solid bold line shows the galvanostatic charge profile of LFP/graphitic carbon during the *in situ* XANES measurements at 0.1C. Dashed lines correspond to the changes in the evaluated "formal valence number" of Fe during the lithiation–delithiation process. The formal valence number of Fe for the composites was calculated by fitting using commercial LiFePO$_4$ powder and FePO$_4$ powder oxidized using the chemical method. The XANES spectra at the iron K-edge of Li$_x$FePO$_4$ rate are shown in three insets. (b) Detailed XRD patterns during the second discharge reactions for the 0.1C rate. The voltage profiles during the measurements are shown on the left.

(runs 36 to 58) cycles, from +2.89 to +2.14. The change in the valence state over one charge–discharge cycle is ± 0.75 corresponding to 128 mA h g^{-1} for LFP, that is 75% of its theoretical capacity.

Based on the results of the XANES study, a reaction mechanism can be proposed:

1st charge: $Li_{0.50}FePO_4 \rightarrow Li_{0.11}FePO_4 + 0.39Li^+ + 0.39e^-$
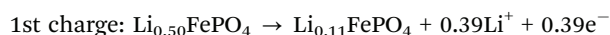
Subsequent cycle: $Li_{0.11}FePO_4 + 0.75Li^+ + 0.75e^- \leftrightarrow Li_{0.86}FePO_4$

The obtained number of exchanged Li from the charge–discharge test (0.82 Li per LFP) and *in situ* XANES measurements (0.75 Li per LFP) is slightly different. This slight difference of <10% could be attributed to the double layer capacitance associated with the surface contribution of the LFP nanoparticle.

Li intercalation in the crystalline phase was further assessed by *in situ* XRD measurements. Fig. 5b (left panel) shows the potential *versus* composition signature of LFP/graphitic carbon during the 1st discharge at 0.1C. Three selected diffraction peaks are presented in Fig. 5b (right panel). The cell was fully charged up to 4.2 V at a slow rate (0.1C) before measurement. At 4.2 V, two peaks are observed at 30.4° and 30.9° that correspond to FePO$_4$ (FP)(211) and (020), respectively. During the discharge reaction, new peaks characteristic of LFP(211) and (020) appear at 29.8° indicating the lithiation reaction in the potential plateau region. Then the peak position and intensity do not change below 3.3 V, while a decrease in the valence state of Fe is observed in this potential region (Fig. 5a) showing that a redox process involving Fe ions occurs in a non-crystalline phase. This confirms the presence of an amorphous phase in the pristine composite that contains most of the Fe^{3+} ions. Accordingly, the capacity in the plateau region can be attributed to the crystalline (c-LFP) phase while the capacity below 3.3 V (sloping region) originates from the amorphous defective LFP phase. The comparison of the capacities calculated in the plateau region (crystalline LFP phase) and in the sloping domain (amorphous defective LFP phase) gives a crystalline/amorphous defective LFP phase of 31/69 by weight (Fig. S10, ESI†). In addition, the peak positions of LFP and FP do not shift during discharge. This indicates that in the crystalline LFP core, Fe^{2+} are located only in undistorted M2 sites and that partial Fe^{2+} lying in distorted M2 sites are located in the amorphous defective LFP phase. This is in fair agreement with the studies showing that crystalline defective LFP is reduced *via* a solid solution mechanism as exhibited by progressive Bragg's peak shifts reported by Amisse *et al.*[33]

In summary, three contributions to the reversible capacity of the LFP/graphitic carbon composite have been identified as (i) c-LFP which shows a constant charge–discharge potential at about 3.4 V; (ii) amorphous defective LFP undergoing a one-phase reaction with a sloping potential profile below 3.4 V; and (iii) double layer capacitance of the graphitic carbon in the entire 2.0–4.2 V potential range.

2.3. Ultrafast charge–discharge behavior

Charge–discharge tests at various current densities (1–480C) were performed (Fig. 6). The LFP/graphitic carbon composite exhibits excellent rate capability, delivering discharge capacities of 89, 60,
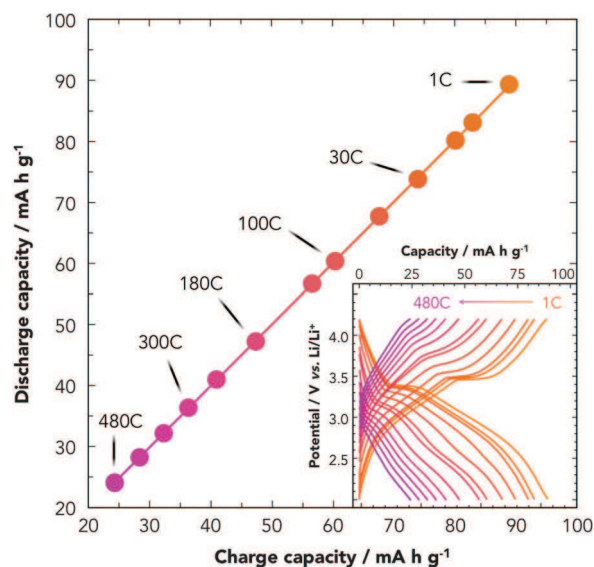

Fig. 6 Plots of discharge capacity *vs.* charge capacity of a half-cell consisting of Li/1 M LiPF$_6$ EC + DEC (LFP/graphitic carbon) composite as a function of C-rate. Inset: Charge–discharge profiles at different charge C-rates from 1 to 480C.

36 and 24 mA h g^{-1} at 1, 100, 300, and 480C rates, respectively, outperforming the reported data in the literature.[25,26,28,35–40] Even more importantly, the LFP/graphitic carbon composite has an extremely high-rate capability in charge as well; it stores 60, 36 and 24 mA h g^{-1} at 100C, 300C, and 480C rate, respectively. Considering that the capacity for the activated carbon (AC) normally used in EDLC devices is typically 40 mA h g^{-1}, the obtained capacity of 60 mA h g^{-1} is still very interesting in the field of supercapacitors. It should be noted, however, that the discharge and charge capacities at each rate show a linear relationship, meaning that the composite can offer a high power density, regardless of the way it is charged or discharged. Such a linear relationship between the charge and discharge capacities highlights the high-power capability of the material in discharge as well as in charge, such as expected for the practical use of hybrid supercapacitors. Such high power performance for both charge and discharge processes is due to the optimized core–shell nanostructure of the LFP/graphitic carbon composites allowing fast Li$^+$ transport. This is confirmed by the calculation of Li$^+$ diffusivity in the materials. We found that the diffusion coefficient of Li$^+$ (D_{Li^+}) in the sloping potential region corresponding to the amorphous LFP phase (Fig. S11, ESI†) is 10^{-11}–10^{-12} cm^2 s^{-1}. This is up to 2 orders of magnitude higher than that of the crystalline LFP phase ($D_{Li^+} = 10^{-13}$ cm^2 s^{-1}) in the plateau region.[41,42] It confirms that the creation of defects or an amorphous phase increases the diffusion coefficient of Li-ions, explaining the high-rate performances.[33]

In addition, extra electrochemical characterization carried out using the uc-LFP (without KB) sample, which did not exhibit the peculiar core–shell structure (Fig. S7a, ESI†), and the composite thermally treated under an air atmosphere to remove the carbon component (Fig. S7c, ESI†) led to degraded electrochemical performances especially without high charge and discharge

capacity (@100C) compared with the core–shell composite (Fig. S7d, ESI†). Therefore, the carbon shell is clearly very important to maintain the peculiar nano-sized "core–shell" structure to sustain ultrafast electrochemical performance. In fact, there are various synthesis parameters that tune the crystalline/amorphous ratio of the LFP phases in the composite. The encapsulated LFP cores did not change essentially by varying annealing time (5 min–2 h) or annealing temperature (700–800 °C) at a fixed ratio of carbon content (50 wt%) (Fig. S12(a), ESI†). However, decreasing the carbon content below 30 wt% (Fig. S12(b), ESI†) drastically increased the LFP particle size, which is not anymore encapsulated. It seems that the carbon content is the factor that affects the size/morphology of the entire composite. Fine-tuning of these parameters would permit designing composite structures with an optimized crystalline/amorphous ratio to get the best electrochemical performance. Systematic studies in this regard are currently under investigation for a follow-up paper.

These peculiar core–shell nanostructured materials offer new opportunities for designing high-rate positive electrodes that can be charged and discharged in a few tens of seconds, for hybrid supercapacitor applications. We have conducted an exploratory test of a full cell configured as AC (20 μm)/1 M LiPF$_6$ (EC + DEC)/ uc-LFP (20 μm) as shown in Fig. S13 (ESI†). The capacity ratio of the anode/cathode was set as 1/1, so the weight ratio of the AC/uc-LFP is 2/1. The voltage range tested was 0–2.7 V at a current density of 34 mA g^{-1} (per LFP). The hybrid full cell delivers 41 F g^{-1}, which is 1.3 times higher than a reference cell (AC/AC in the same electrolyte). This is a small demonstration of a hybrid cell concept and it is feasible for further testing. Note as well that the electrochemical response of the crystalline LFP phase (plateau) is observed, contributing to the improvement of cell capacitance and energy. This validates the proposed concept.

3. Conclusion

Highly dispersed crystal/amorphous LFP nanoparticles encapsulated within hollow-structured graphitic carbon were synthesized using an *in situ* ultracentrifugation process. Ultracentrifugation triggered an *in situ* sol–gel reaction that led to the formation of core–shell LFP/graphitic carbon composite particles. The core–shell structure contains a crystalline LFP (core 1) covered by an amorphous LFP containing Fe^{3+} defects (core 2) that are encapsulated by a graphitic carbon shell. These core–shell LFP nanoparticles show improved Li$^+$ diffusivity thanks to the presence of the amorphous LFP phase. This material enables ultrafast discharge rates (60 mA h g^{-1} at 100C and 36 mA h g^{-1} at 300C) as well as ultrafast charge rates (60 mA h g^{-1} at 100C and 36 mA h g^{-1} at 300C), which offer new opportunities for designing high-energy, ultrafast hybrid supercapacitors.

4. Materials and methods

4.1. Materials

Fe(CH$_3$COO)$_2$ (Aldrich), LiCH$_3$COO (Wako Pure Chemicals) and H$_3$PO$_4$ (Wako Pure Chemicals) were used as the Fe, Li,

and PO$_4$ sources, respectively, while citric acid (C$_6$H$_8$O$_7$) (Aldrich) was used as the chelating agent. Hollow-structured Ketjen Black (KB; EC600JD, Ketjen Black International Company[43]) with 50 nm diameter primary particles with a specific surface area (SSA) of 1270 m^2 g^{-1} was selected as the precursor carbon matrix for encapsulating the nanoscale LFP because of its high electronic conductivity and specific surface area. Ultra-pure water (17 Ω cm) was used as the medium for the entire preparation scheme.

4.2. Preparation of the LFP/graphitic carbon composite by UC treatment

Two different solutions, A and B, were prepared. Solution A contains 0.0837 g (1.00 eq.) of LiCH$_3$COO, 0.2205 g (1.00 eq.) of Fe(CH$_3$COO)$_2$ and 0.2448 g (1.00 eq.) of C$_6$H$_8$O$_7$ dissolved in 7.00 g of H$_2$O. Solution B contains 0.1462 g (1.00 eq.) of H$_3$PO$_4$ dissolved in 14.00 g of H$_2$O. Solution B and 0.200 g of KB were then mixed for 30 min using ultrasonication to obtain a uniform premixture. This premixture was then treated by the first UC for 5 min to form a blackish gel. In this process, PO$_4^{3-}$ uniformly covered the surfaces of the dispersed primary KB carbon particles. After the addition of solution A, a second UC treatment was performed for 5 min. After drying the product at 80 °C for 12 h in a vacuum (ultimate vacuum = 0.67 Pa), the precursor of the LFP/graphitic carbon composite was obtained. A further annealing treatment[44] for 8 min (heating: 3 min, holding 5 min) of 700 °C under a nitrogen flow of the precursor powder led to the obtention of the nano-crystalline LFP/graphitic carbon composite. During these drying and annealing processes, we assume that the water media containing Fe, Li, PO$_4$ sources, and chelating agent (C$_6$H$_8$O$_7$) get concentrated within the hollows of the graphitic carbon shell due to capillary effects leading to the formation of LFP particles in the inner KB instead of outside (Fig. S14, ESI†). Then during annealing at 700 °C, the media evaporates faster in outer shells than inner composite shells. Thereby, the media as well as the LFP-precursor may become more and more concentrated and confined in inner shells. During annealing process, the confined LFP-precursor gets crystallized to become the LFP core part. We also speculate that in the vicinity of outer shells the LFP-precursor has more interference with the graphitic carbons preventing full crystallization resulting in partial crystallized or amorphous phases. Therefore the resulting LFP nanoparticles are configured generally as core crystalline and amorphous outer sphere.

4.3. Physicochemical characterization of the LFP/graphitic carbon composite

Particle size distribution of LFP, the KB-derived graphitic carbon layer, and the nano-structure was carried out by high-resolution transmission electron microscopy (HRTEM, Hitachi H9500 model). X-ray diffraction (XRD, Rigaku SmartLab) was used to characterize the crystalline structure of the LFP/graphitic carbon. The stoichiometry of the composites was determined using thermogravimetric differential thermal analysis (TG/DTA, Seiko Instruments TG/DTA6300) under a synthetic air atmosphere (O$_2$: 20%, N$_2$: 80%). X-ray photoelectron spectroscopy (XPS JEOL Ltd. JPS-9200) was carried out with a pass energy of 40 eV for high-resolution scans

using a monochromated Mg X-ray source. ^{57}Fe Mössbauer spectra were collected in transmission geometry on a constant acceleration spectrometer using a ^{57}Co γ-ray source in a Rh matrix equipped with a cryostat. Velocity and isomer shift (IS) calibrations were performed using α-Fe as a standard at room temperature. Quadrupole splitting (QS) data for each type of Fe ion were analyzed as discrete 0.1 mm s^{-1} step distributions in the 0–6 mm s^{-1} range and then fitted with a Gaussian distribution curve.

4.4. Electrochemical characterization of the LFP/graphic carbon composites

Half-cells were assembled using a negative Li metal electrode and a positive LFP/graphic carbon electrode in 2032 coin-type cells. The electrolyte was a mixture of ethylene carbonate (EC) and diethyl carbonate (DEC) containing 1.0 M lithium hexafluorophosphate (LiPF$_6$). LFP/graphic carbon electrodes were prepared by mixing 90 wt% of the composite and 10 wt% of weight of polyvinylidene difluoride (PVdF) in N-methyl pyrrolidone (NMP). The mixture was coated on an etched-Al foil (current collector) and dried at 80 °C in a vacuum for 12 h. The electrode density, calculated from the loading mass of the composite (2.00 mg) on 1.54 cm^2 of etched Al current collector and the thickness of the LFP/graphic carbon electrode (10 ± 1 μm), was *ca.* 1.30 g cm^{-3}. Charge–discharge tests were performed under constant current mode between 2.0 and 4.2 V *vs.* Li/Li$^+$ at various current densities ranging from 0.1 to 480 C-rate, assuming that 1C-rate equals 170 mA g^{-1}.

4.5. *In situ* XAFS measurements

In situ X-ray adsorption fine structure (XAFS) measurements at the Fe K-edges for the composite samples were performed in transmission mode at the beam line BL14B2 of the synchrotron radiation facility SPring-8 (Hyogo, JAPAN).[45] Laminate-type two-electrode cells (pouch cells) were assembled using lithium metal foil as a negative electrode and the LFP/graphitic carbon composite as a positive electrode. Charge–discharge tests were performed within a 2.0–4.2 V voltage range during the 1st cycle at a rate of 0.1C. XAFS spectra were recorded at equilibrium following a rest period of 20 min at each voltage. The obtained XAFS spectra were analyzed using the spectral fitting software REX2000 (Rigaku Corp.) to evaluate the ratio of Fe species with different oxidation states, such as Fe^{2+} (LFP bulk sample) and Fe^{3+} (FP bulk sample oxidized by the chemical method using NO$_2$BF$_4$).

Acknowledgements

References

1 M. Armand and J. M. Tarascon, *Nature*, 2008, **451**, 652–657.
2 M. D. Slater, D. Kim, E. Lee and C. S. Johnson, *Adv. Funct. Mater.*, 2013, **23**, 947–958.
3 J. M. Tarascon and M. Armand, *Nature*, 2001, **414**, 359–367.
4 P. Simon and Y. Gogotsi, *Nat. Mater.*, 2008, **7**, 845–854.
5 T. Brousse, D. Belanger and J. W. Long, *J. Electrochem. Soc.*, 2015, **162**, A5185–A5189.
6 S. Ardizzone, G. Fregonara and S. Trasatti, *Electrochim. Acta*, 1990, **35**, 263–267.
7 H. Y. Lee and J. B. Goodenough, *J. Solid State Chem.*, 1999, **144**, 220–223.
8 J. W. Lee, A. S. Hall, J.-D. Kim and T. E. Mallouk, *Chem. Mater.*, 2012, **24**, 1158–1164.
9 T. C. Liu, W. G. Pell, B. E. Conway and S. L. Roberson, *J. Electrochem. Soc.*, 1998, **145**, 1882–1888.
10 V. Augustyn, P. Simon and B. Dunn, *Energy Environ. Sci.*, 2014, **7**, 1597.
11 J. Yan, Z. Fan, T. Wei, W. Qian, M. Zhang and F. Wei, *Carbon*, 2010, **48**, 3825–3833.
12 P. Ragupathy, H. N. Vasan and N. Munichandraiah, *J. Electrochem. Soc.*, 2008, **155**, A34.
13 V. Augustyn, J. Come, M. A. Lowe, J. W. Kim, P.-L. Taberna, S. H. Tolbert, H. D. Abruna, P. Simon and B. Dunn, *Nat. Mater.*, 2013, **12**, 518–522.
14 Y.-G. Guo, J.-S. Hu and L.-J. Wan, *Adv. Mater.*, 2008, **20**, 2878–2887.
15 K. Naoi, S. Ishimoto, Y. Isobe and S. Aoyagi, *J. Power Sources*, 2010, **195**, 6250–6254.
16 A. G. Dylla, P. Xiao, G. Henkelman and K. J. Stevenson, *J. Phys. Chem. Lett.*, 2012, **3**, 2015–2019.
17 M. Okubo, E. Hosono, J. Kim, M. Enomoto, N. Kojima, T. Kudo, H. Zhou and I. Honma, *J. Am. Chem. Soc.*, 2007, **129**, 7444–7452.
18 Z. Chen, V. Augustyn, X. Jia, Q. Xiao, B. Dunn and Y. Lu, *ACS Nano*, 2012, **6**, 4319–4327.
19 A. K. Padhi, K. S. Nanjundaswamy, C. Masquelier, S. Okada and J. B. Goodenough, *J. Electrochem. Soc.*, 1997, **144**, 1609–1613.
20 V. Srinivasan and J. Newman, *J. Electrochem. Soc.*, 2004, **151**, A1517–A1529.
21 G. Y. Chen, X. Y. Song and T. J. Richardson, *Electrochem. Solid-State Lett.*, 2006, **9**, A295–A298.
22 S. Y. Chung, J. T. Bloking and Y. M. Chiang, *Nat. Mater.*, 2002, **1**, 123–128.
23 W.-J. Zhang, *J. Power Sources*, 2011, **196**, 2962–2970.
24 X. L. Wu, L. Y. Jiang, F. F. Cao, Y. G. Guo and L. J. Wan, *Adv. Mater.*, 2009, **21**, 2710–2714.
25 K. Zhang, J. T. Lee, P. Li, B. Kang, J. H. Kim, G. R. Yi and J. H. Park, *Nano Lett.*, 2015, **15**, 6756–6763.

26 Z. Chen, Y. Ren, Y. Qin, H. Wu, S. Ma, J. Ren, X. He, Y. K. Sun and K. Amine, *J. Mater. Chem.*, 2011, **21**, 5604–5609.

27 H. Fei, Z. Peng, Y. Yang, L. Li, A.-R. O. Raji, E. L. G. Samuel and J. M. Tour, *Chem. Commun.*, 2014, **50**, 7117–7119.

28 K. Naoi, W. Naoi, S. Aoyagi, J.-I. Miyamoto and T. Kamino, *Acc. Chem. Res.*, 2012, **46**, 1075–1083.

29 K. Kisu, M. Iijima, E. Iwama, M. Saito, Y. Orikasa, W. Naoi and K. Naoi, *J. Mater. Chem. A*, 2014, **2**, 13058–13068.

30 K. Naoi, S. Ishimoto, J.-I. Miyamoto and W. Naoi, *Energy Environ. Sci.*, 2012, **5**, 9363–9373.

31 S.-T. Myung, S. Komaba, N. Hirosaki, H. Yashiro and N. Kumagai, *Electrochim. Acta*, 2004, **49**, 4213–4222.

32 F. Boucher, J. Gaubicher, M. Cuisinier, D. Guyomard and P. Moreau, *J. Am. Chem. Soc.*, 2014, **136**, 9144–9157.

33 R. Amisse, M. T. Sougrati, L. Stievano, C. Davoisne, G. Dražič, B. Budič, R. Dominko and C. Masquelier, *Chem. Mater.*, 2015, **27**, 4261–4273.

34 P. Gibot, M. Casas-Cabanas, L. Laffont, S. Levasseur, P. Carlach, S. Hamelet, J. M. Tarascon and C. Masquelier, *Nat. Mater.*, 2008, **7**, 741–747.

35 M. S. Islam, D. J. Driscoll, C. A. J. Fisher and P. R. Slater, *Chem. Mater.*, 2005, **17**, 5085–5092.

36 J. Liu, M. N. Banis, Q. Sun, A. Lushington, R. Li, T. K. Sham and X. Sun, *Adv. Mater.*, 2014, **26**, 6472–6477.

37 T.-F. Yi, X.-Y. Li, H. Liu, J. Shu, Y.-R. Zhu and R.-S. Zhu, *Ionics*, 2012, **18**, 529–539.

38 B. Wang, A. Liu, W. A. Abdulla, D. Wang and X. S. Zhao, *Nanoscale*, 2015, **7**, 8819–8828.

39 W.-B. Luo, S.-L. Chou, Y.-C. Zhai and H.-K. Liu, *J. Mater. Chem. A*, 2014, **2**, 4927–4931.

40 B. Kang and G. Ceder, *Nature*, 2009, **458**, 190–193.

41 P. P. Prosini, M. Lisi, D. Zane and M. Pasquali, *Solid State Ionics*, 2002, **148**, 45–51.

42 F. Yu, L. Zhang, Y. Li, Y. An, M. Zhu and B. Dai, *RSC Adv.*, 2014, **4**, 54576–54602.

43 Lion Specialty Chemicals Co., Ltd, KETJENBLACK Highly Electro-Conductive Carbon Black, https://www.lion-specialty-chem.co.jp/en/product/carbon/carbon01.htm.

44 K. Kisu, E. Iwama, W. Onishi, S. Nakashima, W. Naoi and K. Naoi, *J. Mater. Chem. A*, 2014, **2**, 20789–20798.

45 Industrial Application Division User Support Group, Japan Synchrotron Radiation Research Institute, SPring-8, http://support.spring8.or.jp/en/index-e.html.